Inorganic Chemistry

Article

pubs.acs.org/IC

Solvate-Dependent Spin Crossover and Exchange in Cobalt(II) Oxazolidine Nitroxide Chelates

Ian A. Gass,[†,‡] Subrata Tewary,[§] Gopalan Rajaraman,[§] Mousa Asadi,[†] David W. Lupton,[†] Boujemaa Moubaraki,[†] Guillaume Chastanet,[∥] Jean-Francois Létard,[∥] and Keith S. Murray*[,†]

[†]School of Chemistry, Monash University, Clayton, Victoria 3800, Australia

[‡]School of Pharmacy and Biomolecular Sciences, University of Brighton, Brighton BN2 4GJ, U.K.

[§]Department of Chemistry, Indian Institute of Technology Bombay, Powai, Mumbai 400076, India

[∥]CNRS, Université de Bordeaux, ICMCB, 87 avenue du Dr. A. Schweitzer, 33608 Pessac, France

Supporting Information

ABSTRACT: Two oxazolidine nitroxide complexes of cobalt(II), $[Co^{II}(L^{\bullet})_2](B(C_6F_5)_4)_2\cdot CH_2Cl_2$ (**1**) and $[Co^{II}(L^{\bullet})_2](B(C_6F_5)_4)_2\cdot 2Et_2O$ (**2**), where, $L^{\bullet}$ is the tridentate chelator 4,4-dimethyl-2,2-bis(2-pyridyl)oxazolidine *N*-oxide, have been investigated by crystallographic, magnetic, reflectivity, and theoretical (DFT) methods. This work follows on from a related study on $[Co^{II}(L^{\bullet})_2](NO_3)_2$ (**3**), a multifunctional complex that simultaneously displays magnetic exchange, spin crossover, and single molecule magnetic features. Changing the anion and the nature of solvation in the present crystalline species leads to significant differences, not only between **1** and **2** but also in comparison to **3**. Structural data at 123 and 273 K, in combination with magnetic data, show that at lower temperatures **1** displays low-spin Co(II)-to-radical exchange with differences in fitted *J* values in comparison to DFT (broken symmetry) calculated *J* values ascribed to the sensitive influence of a tilt angle (θ) formed between the Co(d_{z^2}) and the *trans*-oriented O atoms of the NO radical moieties in $L^{\bullet}$. Spin crossover in **1** is evident at higher temperatures, probably influenced by the solvate molecules and crystal packing arrangement. Complex **2** remains in the high-spin Co(II) state between 2 and 350 K and undergoes antiferromagnetic exchange between Co−radical and radical−radical centers, but it is difficult to quantify. Calculations of the magnetic orbitals, eigenvalue plots, and the spin densities at the Co and radical sites in **1** and **2** have yielded satisfying details on the mechanism of metal−radical and radical−radical exchange, the radical spins being in π^*_{NO} orbitals.

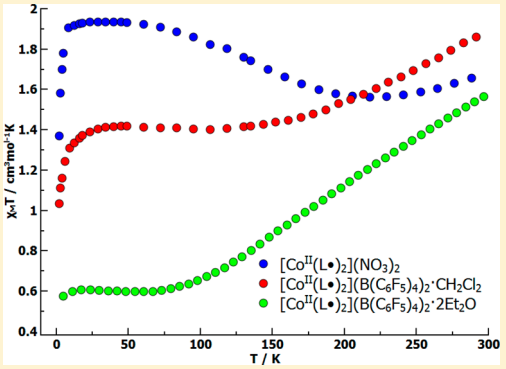

INTRODUCTION

The "metal−radical" approach was pioneered by Gatteschi and co-workers[1] through the use of nitroxide radicals[2] whose weak Lewis base character means they are not expected to coordinate directly to the metal center unless the Lewis acidity of the metal itself is increased by the addition of electron-withdrawing groups such as hexafluoroacetylectonate ($hfac^-$), examples of which include the first single-chain magnet, $[Co^{II}(hfac)_2(rad)]$,[3] and the ferrimagnetically ordered compound $[Mn^{II}(hfac)_2(rad)]$.[4] An alternative approach used to coordinate nitroxides to metal centers involves incorporation of a suitable coordinating group adjacent to the nitroxide radical such as pyrazine, 2,2′-bipyridine, or imidazole.[5] Such metal−radical systems have been extensively studied to gain information on their electronic structure, electron transfer properties, reactivity, and catalytic properties[6] as well as fundamental studies on the type and magnitude of the magnetic exchange interactions to and via a range of transition-metal centers.[1,2]

Multifunctional approaches to spin crossover (SCO) involve the study of the interplay between the spin-crossover properties of a material with a secondary function: for example liquid crystal properties,[7] porosity,[8] and ferromagnetic ordering.[9] Our interest in studying metal complexes using nitroxides stems from our interest in studying the effect of radical−M^{II} (where M = Fe, Co) exchange on the potential of Fe^{II} or Co^{II} to undergo a thermally induced spin transition in a vein similar to the simultaneous spin crossover and exchange seen in a radical $Fe^{III}(SO_4)$ complex[10] and in the cobalt-based dimer $[Co^{II}_2L(NCS)_2(SCN)_2]$, where L is a dinucleating pyridazine-based chelator.[11] We have recently reported simultaneous exchange interactions, spin crossover, reductively induced oxidation, and field-induced slow magnetic relaxation in $[Co^{II}(L^{\bullet})_2](NO_3)_2$ (**3**),[12] where $L^{\bullet}$ is 4,4-dimethyl-2,2-bis(2-pyridyl)oxazolidine *N*-oxide (Figure 1), and have extended this system to a different anion, tetrakis(pentafluorophenyl)borate. Here we report on the synthesis of the two solvated analogues $[Co^{II}(L^{\bullet})_2](B(C_6F_5)_4)_2\cdot CH_2Cl_2$ (**1**) and $[Co^{II}(L^{\bullet})_2](B(C_6F_5)_4)_2\cdot 2Et_2O$ (**2**).

Complex **1** was formed in a manner similar to that for $[Co^{III}(L^-)_2](BPh_4)$[12] using potassium tetrakis(pentafluorophenyl)-borate instead of sodium tetraphenylborate. Complex **1** was

Received: January 15, 2014
Published: May 7, 2014

Downloaded via INDIAN INST OF TECHNOLOGY BOMBAY on November 12, 2020 at 10:37:36 (UTC).
See https://pubs.acs.org/sharingguidelines for options on how to legitimately share published articles.

 © 2014 American Chemical Society dx.doi.org/10.1021/ic5001057 | Inorg. Chem. 2014, 53, 5055−5066

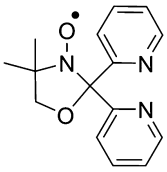

Figure 1. Structural formula of 4,4-dimethyl-2,2-bis(2-pyridyl)-oxazolidine *N*-oxide ($L^{\bullet}$).

synthesized to test the hypothesis that it is the tetraphenylborate anion that is responsible for the one-electron reduction of the dication $[M^{II}(L^{\bullet})_2]^{2+}$ (M = Co,[12] Fe[13]) to form the intermediate $[M^{II}(L^{\bullet})(L^{-})]^{+}$, in which an intramolecular electron transfer takes place to generate the monocationic species $[M^{III}(L^{-})_2]^{+}$. The tetraphenylborate anion can act as a one-electron reductant,[14] whereas the tetrakis(pentafluorophenyl)-borate anion is a very effective noncoordinating anion which should minimize any cation−anion interaction[15] and hence should not act as a reductant toward the $[M^{II}(L^{\bullet})_2]^{2+}$ dication. Therefore, using the tetrakis(pentafluorophenyl)borate instead of the tetraphenylborate anion, in a synthesis similar to that of $[Co^{III}(L^{-})_2](BPh_4)$,[12] should yield the $[M^{II}(L^{\bullet})_2]^{2+}$ dication and not the $[M^{III}(L^{-})_2]^{+}$ monocation, which is a result of a tetraphenylborate-induced reduction. We were particularly interested to see if this anion variation, in combination with solvation/crystal packing variations, would influence the magnetic exchange and spin crossover properties of these materials.

EXPERIMENTAL SECTION

General Considerations. 4,4-Dimethyl-2,2-bis(2-pyridyl)-oxazolidine *N*-oxide ($L^{\bullet}$) was synthesized as described previously.[12,13] All other reagents and solvents were of reagent grade and were used as received. Microanalyses were performed by the Campbell Microanalytical Laboratory, Chemistry Department, University of Otago, Dunedin, New Zealand.

Syntheses. *$[Co^{II}(L^{\bullet})_2](B(C_6F_5)_4)_2\cdot CH_2Cl_2$ (**1**).* A 20 mg portion (0.074 mmol) of 4,4-dimethyl-2,2-bis(2-pyridyl)oxazolidine *N*-oxide ($L^{\bullet}$), 10.4 mg (0.037 mmol) of $Co^{II}(SO_4)\cdot 7H_2O$, and 26.6 mg (0.037 mmol) of $K(B(C_6F_5)_4)$ were dissolved in 10 mL of methanol. After 60 min of stirring, the clear brown solution was evaporated to dryness, the resultant brown precipitate was dissolved in a minimum amount of CH_2Cl_2, and this solution was filtered and diffused with Et_2O to produce X-ray-quality crystals of **1** after 1 day. Yield: 11 mg (27.7%). Anal. Calcd for $C_{79}H_{34}N_6O_4B_2F_{40}Cl_2Co$ (**1**): C, 46.5; H, 1.7; N, 4.1. Found: C, 47.48; H, 2.21; N, 4.25. Thermogravimetric analysis showed a gradual weight of loss of 4.4% between 60 and 90 °C corresponding to the loss of one dichloromethane solvate molecule. IR (ATR, cm^{-1}): 2978 w, 2866 w, 2324 w, 1643 w, 1603 w, 1512 m, 1459 s, 1373 w, 1272 w, 1083 m, 975 s, 773 w, 755 w, 706 w, 683 w, 661 w.

*$[Co^{II}(L^{\bullet})_2](B(C_6F_5)_4)_2\cdot 2Et_2O$ (**2**).* A 20 mg portion (0.074 mmol) of 4,4-dimethyl-2,2-bis(2-pyridyl)oxazolidine *N*-oxide ($L^{\bullet}$), 10.4 mg (0.037 mmol) of $Co^{II}(SO_4)\cdot 7H_2O$, and 53.2 mg (0.074 mmol) of $K(B(C_6F_5)_4)$ were dissolved in 10 mL of methanol. After 60 min of stirring, the clear brown solution was evaporated to dryness, the resultant brown precipitate was dissolved in a minimum amount of CH_2Cl_2, and this solution was filtered and diffused with Et_2O to produce X-ray-quality crystals of **2** after 1 day. Yield: 25 mg (49.7%). Anal. Calcd for $C_{86}H_{52}N_6O_6B_2F_{40}Co$ (**2**): C, 49.1; H, 2.5; N, 4.0. Found: C, 48.26; H, 2.26; N, 3.93. Thermogravimetric analysis showed a gradual weight of loss of 8.1% between 65 and 90 °C corresponding to the loss of two diethyl ether solvate molecules. IR (ATR, cm^{-1}): 2978 w, 2867 w, 2325 w, 1642 w, 1603 w, 1512 m, 1459 s, 1373 w, 1272 w, 1083 m, 975 s, 772 w, 756 w, 706 w, 683 w, 660 w.

Magnetic Susceptibility Measurements. Variable-temperature magnetic susceptibility measurements were performed on a Quantum Design MPMS 7T SQUID magnetometer over the temperature range 2−340 K for **1** and 5−340 K for **2** in an applied DC field of 0.5 T. The SQUID magnetometer was calibrated by use of a standard palladium sample (Quantum Design) of accurately known magnetization or by use of a magnetochemical calibrant such as $CuSO_4\cdot 5H_2O$. Microcrystalline samples were dispersed in Vaseline in order to avoid torquing of the crystallites. The sample mulls were contained in a calibrated capsule held at the center of a drinking straw that was fixed at the end of the sample rod.

Optical Reflectivity Measurements. These measurements were performed using a home-built instrument coupled with a CVI spectrometer. This equipment can collect the reflectivity spectra in the 450−950 nm range at a given temperature and also follow the temperature dependence of the signal at a selected wavelength (±2.5 nm) between 5 and 290 K. The instrument is also equipped with an optical detector, which collected the whole reflected intensity and gave the total reflectivity signal as a function of temperature. The source of white light consisted of a halogen lamp emitting between 300 and 2400 nm. This analysis was performed directly on a thin layer of the solid samples in the form of a polycrystalline powder of **1** and **2** without any dispersion in a matrix.

Thermogravimetric Analysis. Thermogravimetric analysis measurements on **1** and **2** were performed on a Mettler Toledo TGA/DSC STAR^e system at a rate of 5 °C min^{-1} from 25 to 550 °C using standard 40 μL aluminum pans. Data from a blank run using a standard 40 μL aluminum pan (5 °C min^{-1} from 25 to 550 °C) was subtracted from the resultant data for **1** and **2** to compensate for the gradual weight rise seen for the pans alone.

DFT Calculations. DFT[16] calculations using the Gaussian 09 suite of programs[17] were carried out on the X-ray crystal structures of **1** and **2**. Magnetic exchange coupling constant (J) values were calculated using the broken symmetry approach developed by Ginsberg and Noodleman.[18] The B3LYP[19] functional, which has proven to be good for obtaining numerical estimates of magnetic exchange in a variety of transition metals, lanthanides, and metal−radical complexes, was employed in our study.[20−22] However, there are also instances where B3LYP has failed to reproduce the correct ground state, especially in the case of our previous study on LS Fe(II) with the same ligand system.[23] The Ahlrichs triple-ζ valence (TZV)[24] basis set as implemented in G09 was used for all the elements. We have adopted the $^{mult}complex_{spin\ state}$ notation for our study to differentiate various spin states arising from different modes of exchange coupling and the spin state of the metal ions. In the above notation, mult in the superscript denotes the total multiplicity, while the spin state in the subscript denotes the nature of the spin state (low spin (LS) or high spin (HS)) at the Co(II) center. The spin density plots and MO diagrams were generated using Chemcraft version 1.6.[25]

X-ray Crystallography. X-ray crystallographic measurements on **1** and **2** were performed at 123(2) K (**1**·123 K, **2**·123 K) and 273(2) K (**1**·273 K, **2**·273 K) using a Bruker Smart Apex X8 diffractometer with Mo Kα radiation (λ = 0.7107 Å). Single crystals were mounted on a glass fiber using oil for the 123 K collections with the same crystals then glued on to a glass rod and encased with Araldite for the 273 K collections. Crystallographic data and refinement parameters for **1** and **2**, given in Table 1, were solved by direct methods (SHELXS-97) and refined (SHELXL-97) by full least squares on all F^2 data.[26] In complexes **1**·123 K and **1**·273 K the asymmetric unit contains the cobalt monomer, two tetrakis(pentafluorophenyl)borate anions, and one dichloromethane solvate molecule. In **2**·123 K the asymmetric unit contains half the cobalt monomer, one tetrakis(pentafluorophenyl)-borate anion, and two half-occupied diethyl ether solvate molecules. The O4−C46 and C46−C47 bond lengths were restrained to 1.420 and 1.520 Å, respectively, with the DFIX command. **2**·273 K contains half of the cobalt monomer and one tetrakis(pentafluorophenyl)borate anion. There is some residual electron density in **2**·273 K which could not be modeled unambiguously; therefore, SQUEEZE[27] was applied, resulting in an electron count of 264 electrons per cobalt complex with a void volume of 583 Å^3. The same crystal used in **2**·123 K was encased in Araldite and used for the 273 K collection (**2**·273 K). In **2**·123 K there are four half-occupied diethyl ether solvate molecules per complex. Each diethyl ether contributes 42 electrons; thus, **2**·273 K

dx.doi.org/10.1021/ic5001057 | Inorg. Chem. 2014, 53, 5055−5066

Table 1. Crystallographic Data for 1·123 K, 1·273 K, 2·123 K, and 2·273 K

	1·123 K	1·273 K	2·123 K	2·273 K
formula	$C_{79}H_{34}N_6O_4B_2Cl_2F_{40}Co$	$C_{79}H_{34}N_6O_4B_2Cl_2F_{40}Co$	$C_{86}H_{52}N_6O_6B_2F_{40}Co$	$C_{78}H_{32}N_6O_4B_2F_{40}Co$
M_r	2042.57	2042.57	2105.89	1957.65
cryst syst	triclinic	triclinic	triclinic	triclinic
space group	$P\bar{1}$	$P\bar{1}$	$P\bar{1}$	$P\bar{1}$
a/Å	13.0222(7)	13.1755(9)	12.8991(6)	13.087(2)
b/Å	14.0488(8)	14.1877(11)	13.7949(6)	13.948(3)
c/Å	22.9888(14)	23.3401(17)	14.2008(8)	14.375(3)
α/deg	90.156(2)	90.191(2)	87.8470(10)	87.501(7)
β/deg	95.968(2)	96.024(3)	77.6540(10)	77.561(8)
γ/deg	113.680(2)	113.510(2)	66.158(2)	65.573(6)
V/Å^3	3826.2(4)	3973.8(5)	2254.45(19)	2330.0(8)
T/K	123(2)	273(2)	123(2)	273(2)
Z	2	2	1	1
ρ_{calcd}/g cm^{-3}	1.773	1.707	1.551	1.395
λ^a/Å	0.71073	0.71073	0.71073	0.71073
no. of indep rflns	17491	17968	10172	10516
no. of rflns with $I > 2\sigma(I)$	11332	8496	6961	4138
no. of params	1211	1211	689	588
no. of restraints	0	0	2	0
final R1, wR2^b ($I > 2\sigma(I)$)	0.0501, 0.1113	0.0680, 001 475	0.0637, 0.1709	0.0693, 0.1714
R1, wR2^b (all data)	0.0928, 0.1295	0.1652, 0.1893	0.0979, 0.1992	0.1462, 0.1907
goodness of fit	1.024	0.998	1.046	0.825
largest residuals/e Å^{-3}	0.727, −0.888	0.533, −0.500	0.983, −0.756	0.540, −0.494

^{a}Graphite monochromators. $^b R1 = \Sigma||F_0| - |F_c||/\Sigma|F_0|$, $wR2 = \{\Sigma[w(F_0^2\Sigma F_c^2)^2]/\Sigma[w(F_0^2)]\}^{1/2}$.

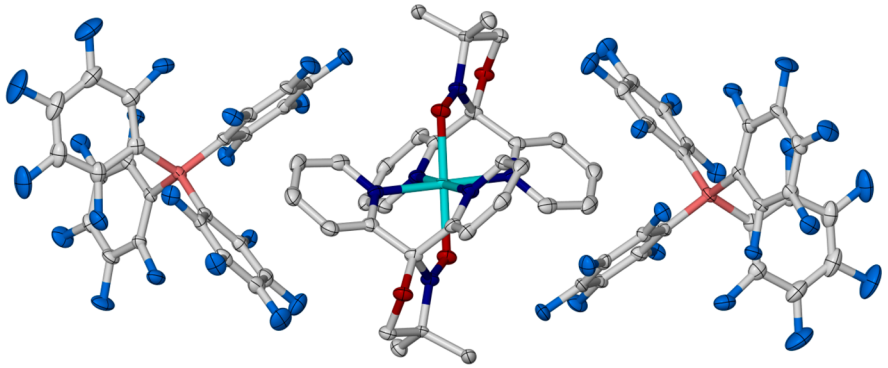

Figure 2. Molecular structure of **1**·123 K. The structure in **1**·123 K is representative of **1**·273 K. Hydrogen atoms and dichloromethane solvate are omitted for clarity. Color code: oxygen, red; nitrogen, dark blue; boron, orange; fluorine, light blue; cobalt, turquoise.

can only show a maximum of 84 electrons per cobalt complex. The value of 264 electrons per cobalt complex is therefore nonsensical and is likely a result of weak high-angle data, of which SQUEEZE[27] is highly dependent. As a useful comparison SQUEEZE[27] was applied to the collection at 123 K (**2**·123 K) with unmodeled solvent peaks, giving a void volume of 541 Å^3 and 226 electrons per cobalt complex. The void volumes are comparable between **2**·123 K and **2**·273 K given the temperature variation, which suggests it is likely the unmodeled electron density in **2**·273 K that corresponds to two diethyl ethers per cobalt complex. For complexes **1** and **2** all non-hydrogen atoms have been refined anisotropically and all hydrogens have been placed in calculated positions. Full crystallographic data have been deposited with the Cambridge Crystallographic Data Centre, 12 Union Road, Cambridge CB2 1EZ, U.K. (http://www.ccdc.cam.ac.uk/) as CCDC numbers 979747−979750.

RESULTS AND DISCUSSION

Synthesis and Structure. $[Co^{II}(L^{\bullet})_2](B(C_6F_5)_4)_2\cdot CH_2Cl_2$ (**1**) was isolated by reacting 4,4-dimethyl-2,2-bis(2-pyridyl)-oxazolidine *N*-oxide ($L^{\bullet}$), $Co^{II}SO_4\cdot 6H_2O$, and $K(B(C_6F_5)_4)$ in a 2:1:1 ratio in MeOH. Evaporation of this methanolic solution yielded a brown precipitate, which was then dissolved in a minimum amount of dichloromethane and diffused with Et_2O to produce crystalline **1** in approximately 30% yield. $[Co^{II}(L^{\bullet})_2](B(C_6F_5)_4)_2\cdot 2Et_2O$ (**2**) was isolated in a manner similar to that for **1**, but changing the $L^{\bullet}$:$Co^{II}SO_4\cdot 7H_2O$:$K(B(C_6F_5)_4)$ ratio to 2:1:2 resulted in crystalline **2** in approximately 50% yield. In complexes **1**·123 K and **1**·273 K the asymmetric unit contains the cobalt monomer, two tetrakis(pentafluorophenyl)borate anions, and one dichloromethane solvate molecule (Figure 2). In **2**·123 K the asymmetric unit contains half of the cobalt monomer, one tetrakis(pentafluorophenyl)borate anion, and two half-occupied diethyl ether solvate molecules (Figure 3). In the **2**·273 K crystal structure there is some residual electron density which could not be modeled unambiguously, but it is likely to represent two diethyl ether molecules as in the **2**·123 K case (vide supra).

The complexes at various temperatures, viz. **1**·123 K, **1**·273 K, **2**·123 K, and **2**·273 K, crystallize in the same triclinic space

dx.doi.org/10.1021/ic5001057 | Inorg. Chem. 2014, 53, 5055−5066

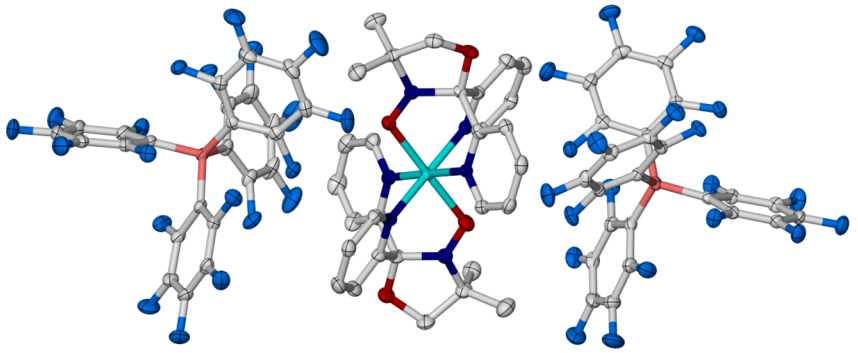

Figure 3. Molecular structure of **2**·123 K. The structure in **2**·123 K is representative of that of **2**·273 K. Hydrogen atoms and diethyl ether solvate molecules are omitted for clarity. Color code: oxygen, red; nitrogen, dark blue; boron, orange; fluorine, light blue; cobalt, turquoise.

group, $P\bar{1}$. An inversion center sits on the cobalt in **2**, generating the $[Co^{II}(L^{\bullet})_2]^{2+}$ dication. The $[Co^{II}(L^{\bullet})_2]^{2+}$ dications in **1** and **2** are structurally similar with a slight variation in bond lengths and angles, which, along with magnetic studies (vide infra), help us to assign the oxidation and spin states of the central cobalt ion as well as assignment of the neutral radical ($L^{\bullet}$) form of the ligand.

Each *mer*-tridentate ligand coordinates to the cobalt ion equatorially via two pyridyl donors and axially via the oxygen completing the coordination sphere (Figure 4). In **1**·123 K

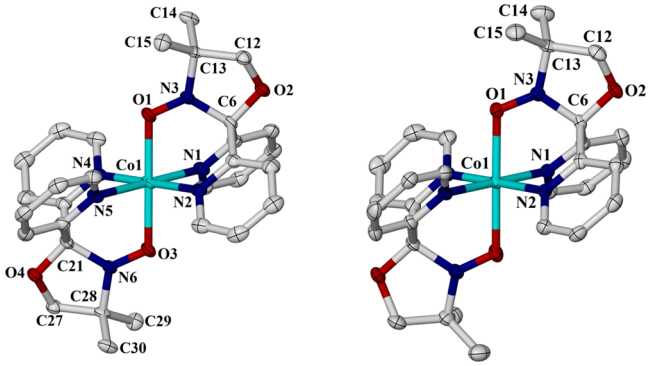

Figure 4. Molecular structures of the dication $[Co^{II}(L^{\bullet})_2]^{2+}$ in **1**·123 K (left) and **2**·123 K (right). The structure and atomic labeling in **1**·123 K and **2**·123 K are representative of those of **1**·273 K and **2**·273 K. Color code: oxygen, red; nitrogen, dark blue; cobalt, turquoise.

this results in an axially elongated octahedral geometry (cis, 86.54(9)−93.90(9)°; trans, 178.94(8)−179.51(10)°; Co−O 2.117(2), 2.126(2) Å, Co−N 1.977(2), 1.981(2), 1.987(2), 1.992(2) Å). This axial elongation disappears upon heating to 273 K (**1**·273 K, Figure 5) with a significant increase in the Co−N bond lengths accompanied by a slight decrease in the Co−O bond lengths resulting in a more perfectly realized octahedral geometry (cis, 85.07(13)−95.97(13)°; trans, 178.90(13)−179.29(12)°; Co−O 2.078(3), 2.086(3) Å, Co−N 1.977(2), 1.981(2), 1.987(2), 1.992(2) Å). The nitroxide N−O bond lengths are 1.274(3) and 1.276(3) Å in **1**·123 K and 1.275(4) and 1.278(4) Å in **1**·273 K (Table 2 and Figure 5). In **1**·123 K and **1**·273 K there are two tetrakis(pentafluorophenyl)-borate anions and one dichloromethane solvate molecule per dication with no significant intermolecular interactions present. On the basis of the centroid calculated between the nitroxide nitrogen and oxygen the shortest distance between neighboring nitroxide groups is 9.640 Å in **1**·123 K and 9.728 Å in **1**·273 K

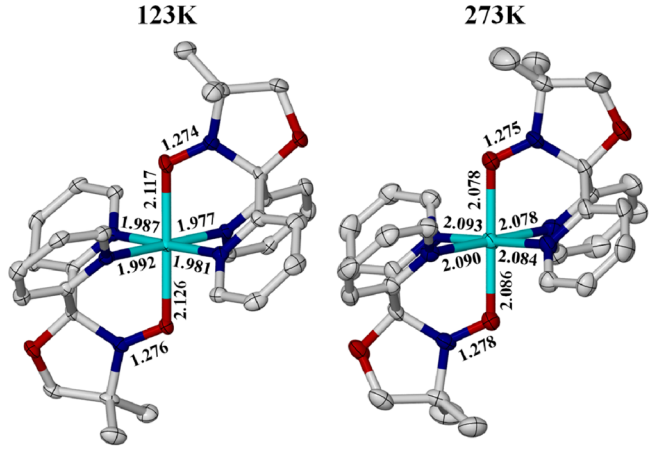

Figure 5. Molecular structure of the dication $[Co^{II}(L^{\bullet})_2]^{2+}$ in **1**·123 K (left) and **1**·273 K (right) with relevant bond lengths quoted in Å without uncertainties (see Table 2). Hydrogen atoms and anions are omitted for clarity. Color code: oxygen, red; nitrogen, dark blue; cobalt, turquoise.

while the shortest Co−Co distance is 11.738 Å in **1**·123 K and 11.950 Å in **1**·273 K (Table 3).

Complex **2** at both temperatures, i.e. **2**·123 K and **2**·273 K, shows slightly distorted octahedral geometries with no significant distortions in the axial or equatorial directions (cis, 85.83(11)−94.17(11)°; trans, all 180°; Co−O 2.054(2)−2.075(2) Å, Co−N 2.098(3)−2.116(3) Å). The nitroxide N−O bond lengths are 1.286(4) Å in **2**·123 K and 1.290(3) Å in **2**·273 K (Table 4 and Figure 6). In **2**·123 K and **2**·273 K there are two tetrakis(pentafluorophenyl)borate anions and two diethyl ether solvate molecules per dication with no significant intermolecular interactions present. The shortest distance between neighboring nitroxide groups is 10.090 Å in **2**·123 K and 10.143 Å in **2**·273 K, while the shortest Co−Co distance is 12.899 Å in **2**·123 K and 13.087 Å in **2**·273 K (Table 3). The different solvate molecules in **1** and **2** effect different packing arrangements, as seen in Figure S3 (see Supporting Information), with **1** having shorter distances between neighboring nitroxide groups and shorter Co−Co distances than **2** (Table 3).

There is an unambiguous pseudo-Jahn−Teller distortion in **1**·123 K, which strongly suggests we have a low-spin octahedral Co(II) (d^7) ion at 123 K. This strong pseudo-Jahn−Teller distortion is useful in differentiating the low-spin $^2E(t_{2g}^6e_g^1)$ and high-spin $^4T_1(t_{2g}^5e_g^2)$ states of Co(II), where the presence of such a distortion can be identified easily by crystallographic studies. In **1**·273 K the pseudo Jahn−Teller distortion has

dx.doi.org/10.1021/ic5001057 | *Inorg. Chem.* 2014, 53, 5055−5066

Table 2. Selected Bond Lengths (Å), Bond Angles (deg), and Torsion Angles (deg) for $[Co^{II}(L^{\bullet})_2]^{2+}$ in 1·123 K and 1·273 K

	1·123 K	1·273 K
Co(1)−O(1)	2.117(2)	2.078(3)
Co(1)−N(1)	1.977(2)	2.078(4)
Co(1)−N(2)	1.981(2)	2.084(3)
Co(1)−O(3)	2.126(2)	2.086(3)
Co(1)−N(4)	1.987(2)	2.093(3)
Co(1)−N(5)	1.992(2)	2.090(3)
O(1)−N(3)	1.274(3)	1.275(4)
O(3)−N(6)	1.276(3)	1.278(4)
N(3)−C(6)	1.478(4)	1.472(5)
N(3)−C(13)	1.473(4)	1.474(5)
C(6)−O(2)	1.395(3)	1.392(5)
O(2)−C(12)	1.452(4)	1.429(6)
C(12)−C(13)	1.516(4)	1.507(7)
C(13)−C(14)	1.516(4)	1.544(7)
C(13)−C(15)	1.537(4)	1.493(7)
N(6)−C(21)	1.488(4)	1.491(5)
N(6)−C(28)	1.480(4)	1.482(5)
C(21)−O(4)	1.395(3)	1.399(5)
O(4)−C(27)	1.446(3)	1.448(5)
C(27)−C(28)	1.520(4)	1.518(6)
C(28)−C(29)	1.515(4)	1.522(6)
C(28)−C(30)	1.527(4)	1.506(6)
Co(1)−O(1)−N(3)	114.73(17)	116.5(2)
Co(1)−O(3)−N(6)	113.40(16)	115.3(2)
Co(1)−O(1)−N(3)−C(6)	−7.4	1.9
Co(1)−O(1)−N(3)−C(13)	−168.8	170.7
Co(1)−O(3)−N(6)−C(21)	−1.7	2.1
Co(1)−O(3)−N(6)−C(28)	−174.1	−175.8

Table 3. Shortest Nitroxide NO···NO and Co···Co Distances (Å) between Neighboring Dications in 1 and 2

	1·123 K	1·273 K	2·123 K	2·273 K
NO··NO	9.640	9.728	10.090	10.143
Co··Co	11.738	11.950	12.899	13.087

disappeared and the bond lengths are consistent with the expectation for high-spin Co(II) (Figure 5), leading us to conclude that this temperature-dependent behavior is consistent with a gradual spin crossover. The average bond length difference around the octahedral Co(II) ion at 123 and 273 K is 0.055 Å slightly lower than the range 0.07−0.11 Å expected for a complete spin crossover,[28] suggesting the spin crossover is incomplete at 273 K. This is borne out by magnetic susceptibility measurements (vide infra). The bond lengths and absence of any Jahn−Teller distortions in **2**·123 K and **2**·273 K suggest that the central Co(II) ion remains high spin throughout the temperature range studied (Figure 6). The nitroxide N−O bond lengths of 1.274(3) and 1.276(3) Å in **1**·123 K, 1.275(4) and 1.278(4) Å in **1**·273 K, 1.286(4) Å in **2**·123 K, and 1.290(3) Å in **2**·273 K suggest that the ligands are all in the neutral radical form ($L^{\bullet}$).[12,13] We can therefore assign a gradual Co(II) spin crossover with two neutral radical ligands in **1** ($[Co^{II}(L^{\bullet})_2](B(C_6F_5)_4)_2{\cdot}CH_2Cl_2$) and a high-spin Co(II) ion with two neutral radical ligands in **2** ($[Co^{II}(L^{\bullet})_2](B(C_6F_5)_4)_2{\cdot}2Et_2O$) on the crystallographic data alone, and this is confirmed

Table 4. Selected Bond Lengths (Å), Bond Angles (deg), and Torsion Angles (deg) for $[Co^{II}(L^{\bullet})_2]^{2+}$ in 2·123 K and 2·273 K

	2·123 K	2·273 K
Co(1)−O(1)	2.054(2)	2.075(2)
Co(1)−N(1)	2.114(3)	2.098(3)
Co(1)−N(2)	2.116(3)	2.107(3)
O(1)−N(3)	1.286(4)	1.290(3)
N(3)−C(6)	1.489(4)	1.465(4)
N(3)−C(13)	1.487(4)	1.484(4)
C(6)−O(2)	1.393(4)	1.397(4)
O(2)−C(12)	1.459(4)	1.440(4)
C(12)−C(13)	1.517(5)	1.519(5)
C(13)−C(14)	1.525(4)	1.518(5)
C(13)−C(15)	1.520(5)	1.506(6)
Co(1)−O(1)−N(3)	115.4(2)	114.37(19)
Co(1)−O(1)−N(3)−C(6)	6.3	−4.1
Co(1)−O(1)−N(3)−C(13)	−169.5	172.8

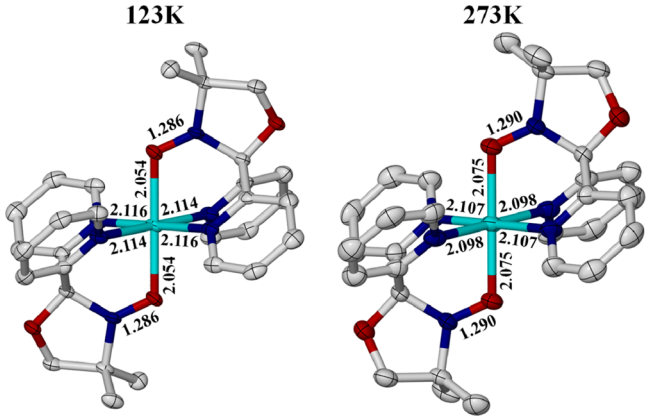

Figure 6. Molecular structure of the dication $[Co^{II}(L^{\bullet})_2]^{2+}$ in **2**·123 K (left) and **2**·273 K (right) with relevant bond lengths quoted in Å without uncertainties (Table 4). Hydrogen atoms and anions are omitted for clarity.Color code: oxygen, red; nitrogen, dark blue; cobalt, turquoise.

by magnetic susceptibility measurements and DFT calculations (vide infra).

Magnetic Studies. DC magnetic susceptibilities were performed on crystals of **1** in the 2−340 K range (Figure 7). For complex **1** the $\chi_M T$ value of 2.10 $cm^3\ mol^{-1}$ K at 340 K decreases slowly upon cooling to a $\chi_M T$ value of 1.41 $cm^3\ mol^{-1}$ K at 130 K, which forms a plateau down to 28.8 K, whereupon it then decreases rapidly upon cooling, finally reaching a $\chi_M T$ value of 1.03 $cm^3\ mol^{-1}$ K at 2 K. The rapid decrease from 28.8 K down to 2 K is likely due to thermal depopulation via Zeeman splitting of the $S = {}^1/_2$ state and close-lying $S = {}^3/_2$ state (Figure 7) with some additional zero-field splitting of the $S = {}^3/_2$ state. The constant $\chi_M T$ value of around 1.41 $cm^3\ mol^{-1}$ K within the plateau region between 130−28.8 K clearly does not correspond to isolated $S = {}^1/_2$ (0.375 $cm^3\ mol^{-1}$ K) or $S = {}^3/_2$ (1.875 $cm^3\ mol^{-1}$ K) ground state $\chi_M T$ values (assuming g = 2.00). This suggests the possibility of at least one weak exchange pathway leading to close lying $S = {}^1/_2$ and $S = {}^3/_2$ states. The spin Hamiltonian describing the exchange interactions in **1** is given by eq 1, where $\hat{S}_1$ and $\hat{S}_3$ are the radical nitroxide spins and $\hat{S}_2$ is the low-spin Co(II) ion. Using the Kambe vector

dx.doi.org/10.1021/ic5001057 | Inorg. Chem. 2014, 53, 5055−5066

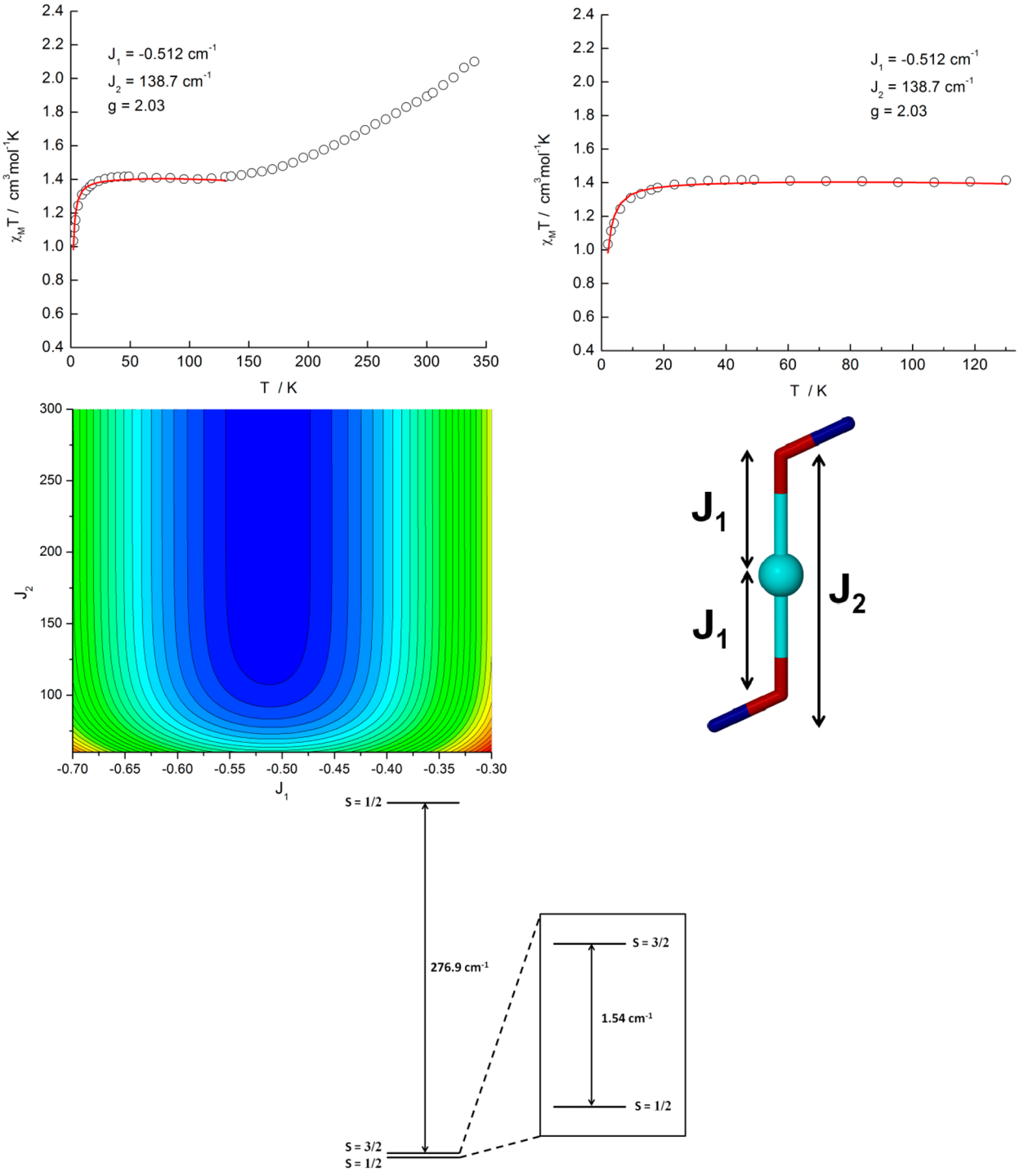

Figure 7. Plots of $\chi_M T$ vs T for **1** in the temperature ranges 2−340 K (top left) and 2−130 K (top right), contour plot of J_1 vs J_2 with lowest residual in blue (middle left), exchange interaction model (middle right), and spin energy levels (bottom). The solid red line (top left and right) represents a fit of the experimental data in the temperature range 2−130 K to the exchange interaction model shown (middle right).

$$\hat{H} = -2J_1(\hat{S}_1\hat{S}_2 + \hat{S}_2\hat{S}_3) - 2J_2(\hat{S}_1\hat{S}_3) \quad (1)$$

coupling method,[29] we can determine the eigenvalues of eq 1 by using the substitutions $\hat{S}_A = \hat{S}_1 + \hat{S}_3$ and $\hat{S}_T = \hat{S}_A + \hat{S}_2$ to form eq 2,

$$\hat{H} = -J_1(\hat{S}_T^{\,2} - \hat{S}_A^{\,2} - \hat{S}_2^{\,2}) - J_2(\hat{S}_A^{\,2} - \hat{S}_1^{\,2} - \hat{S}_3^{\,2}) \quad (2)$$

whose eigenvalues can be represented by combinations of S_A and S_T as in eq 3. This leads to a 3-fold multiplicity of the spin system

$$E(S_T,S_A) = -J_1[S_T(S_T + 1) - S_A(S_A + 1) - {}^3/_4] - J_2[S_A(S_A + 1) - {}^3/_2] \quad (3)$$

with two $S = {}^1/_2$ spin states and one $S = {}^3/_2$ spin state with their relative energies shown in Table 5. The χ_MT vs T data between 2 and 130 K could be fitted satisfactorily with the program PHI[30] using a 2J trimer model (Figure 7), with the spin Hamiltonian shown in eq 1 yielding the best-fit parameters: $J_1 = -0.512$ cm^{-1}, $J_2 = +138.7$ cm^{-1}, and $g = 2.03$ (Figure 7). The contour plot of

dx.doi.org/10.1021/ic5001057 | Inorg. Chem. 2014, 53, 5055−5066

Table 5. Possible Spin States for a Linear Trimer with $S_1 = S_2 = S_3 = {}^1/_2$

S_A	S_2	S_T	$E(S_T,S_A)$
0	${}^1/_2$	${}^1/_2$	${}^3/_2J_2$
1	${}^1/_2$	${}^3/_2$	$-J_1 - {}^1/_2J_2$
		${}^1/_2$	$2J_1 - {}^1/_2J_2$

J_1 vs J_2 in Figure 7 shows the lowest residual values of this fit in blue, and a clear minimum valley can be seen, highlighting the sensitivity of J_1 and insensitivity of the magnitude of J_2 to the fit. The J_2 value of 138.7 cm^{-1} reported is essentially a minimum value of J_2, and equally good fits can be reproduced with larger J_2 values. Therefore, it is best to view these fitted J values as weakly antiferromagnetic for J_1 and strongly ferromagnetic for J_2. The small antiferromagnetic exchange between the nitroxide radical and the low-spin Co(II) ion (J_1) and large ferromagnetic radical−radical exchange (J_2) stabilizes a $S = {}^1/_2$ ground state with the $S = {}^3/_2$ excited state lying only 1.54 cm^{-1} higher in energy, a direct consequence of the comparatively small value of J_1. The large and positive value of J_2 results in the next excited $S = {}^1/_2$ state some 276.9 cm^{-1} above the $S = {}^3/_2$ first excited state (Figure 7). Alternative χ_MT vs T fits can be found in Figures S5−S10 in the Supporting Information. The M vs H data could be fitted satisfactorily with PHI[30] using the giant spin approximation with $S = {}^3/_2$ (Figures S11−S13 in the Supporting Information), yielding the parameters $g = 1.98$ and $D = +24.21$ cm^{-1}, where the corresponding Hamiltonian is given by eq 4, where D is the axial anisotropy zfs parameter, μ_B is the Bohr magneton, S_z^2 is the easy-axis spin operator, and B is the applied field.

$$\hat{H} = DS_z^2 + E(S_x^2 - S_y^2) + g\mu_B\vec{B}\cdot\vec{S} \quad (4)$$

This fit, however, only considers low-temperature/high-field data and does not account for the plateau in the $\chi_M T$ vs T plot at 1.41 cm^3 mol^{-1} K between 130 and 28.8 K, indicative of close-lying $S = {}^1/_2$ and $S = {}^3/_2$ ground and excited states. Simulations of $\chi_M T$ vs T plots using PHI[30] for an isolated $S = {}^3/_2$ with D values ranging from 0−90 cm^{-1} are shown in Figure S14 (see the Supporting Information) and highlight the fact that an isolated $S = {}^3/_2$ system with a large range of D values cannot reproduce the $\chi_M T$ vs T plateau at 1.41 cm^3 mol^{-1} K between 130 and 28.8 K. It is therefore highly probable that we have a small antiferromagnetic exchange between the nitroxide radical and the low-spin Co(II) ion (J_1) and a large ferromagnetic radical−radical exchange (J_2) stabilizing a $S = {}^1/_2$ ground state with a close -lying $S = {}^3/_2$ excited state.

It seems to be counterintuitive that the radical−radical superexchange interaction (J_2 = 138.7 cm^{-1}) via the low-spin Co(II) ion is orders of magnitude greater than the shorter direct exchange between the radical and the Co(II) ion (J_1 = −0.512 cm^{-1}), but we have previously reported a large and negative antiferromagnetic radical−radical exchange (J = −315 cm^{-1} using the spin Hamiltonian $\hat{H} = -2J\hat{S}_1\hat{S}_2$) via a low-spin Fe(II) ion in $[Fe^{II}(L^{\bullet})_2](BF_4)_2$[13] and a large ferromagnetic radical−radical exchange (J_2 = 63.9 cm^{-1} using the spin Hamiltonian $\hat{H} = -2J_1(\hat{S}_1\hat{S}_2 + \hat{S}_2\hat{S}_3) - 2J_2(\hat{S}_1\hat{S}_3)$) in $[Co^{II}(L^{\bullet})_2](NO_3)_2$ (**3**).[12] Clearly the mechanism of the radical−radical superexchange is dependent on the electronic properties associated with the transition-metal ion in question, whose magnetic orbital distribution will result in differing degrees of overlap with the nitroxide π^* orbital. This leads to a large radical−radical antiferromagnetic exchange when the metal ion is low-spin Fe(II)[13] and a large radical−radical ferromagnetic interaction with low-spin Co(II).[12] There is a significant difference, however, in the radical to low-spin octahedral Co(II) exchange interaction in **1** (J_1 = −0.512 cm^{-1} using eq 1) in comparison to the previously reported complex $[Co^{II}(L^{\bullet})_2](NO_3)_2$ (**3**)[12] (J_1 = +63.8 cm^{-1} using eq 1) at temperatures below 130 K. The comparison between complexes **1** and **3** (Figure S4 and Table S1 in the Supporting Information) is discussed further in a DFT theoretical study (vide infra).

The previous fits and discussion on **1** have been based on the magnetic data observed below 130 K, since spin crossover and emergence of the HS Co(II) state occurs at higher temperatures. As the temperature is increased above 130 K, we see a gradual increase in the $\chi_M T$ values from 1.41 cm^3 mol^{-1} K at 130 K to 2.10 cm^3 mol^{-1} K at 340 K. This is consistent with a gradual, incomplete Co(II) spin-crossover transition in a similar vein to the spin-crossover behavior we reported for the analogous compound **3**. Magnetic susceptibility measurements remain the most useful technique in monitoring the Co(II) spin crossover; however, the ability to extract any useful information from the high-temperature (>130 K) $\chi_M T$ vs T plots is made difficult in **1**, where we have simultaneous spin crossover, exchange, and temperature-dependent HS Co(II) behavior. Therefore, at best, we can only conclude that we have a gradual, incomplete spin crossover. This behavior is consistent with variable-temperature crystallographic measurements, which show a clear axial Jahn−Teller distortion at 123 K (**1**·123 K, Figure 5) associated with a LS Co(II) ion. Upon heating this axial distortion disappears and the bond lengths are consistent with the expectation for HS Co(II) (**1**·273 K, Figure 5), confirming the spin-crossover transition.

DC magnetic susceptibilities were measured on crystals of **2** in the 5−340 K range under an applied field of 0.5 T (Figure 8).

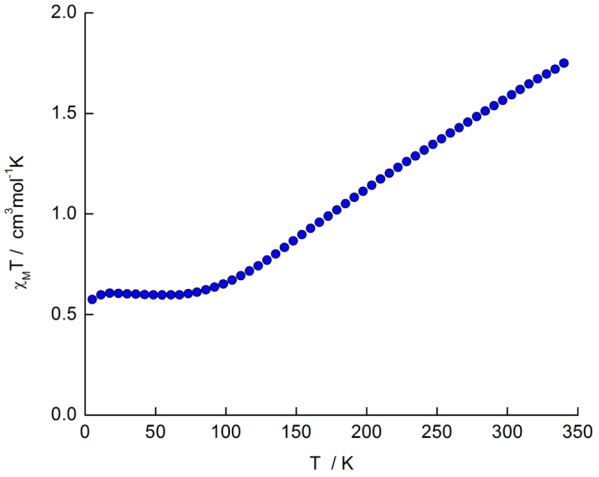

Figure 8. Plot of $\chi_M T$ vs T for **2**.

For complex **2** the $\chi_M T$ value of 1.75 cm^3 mol^{-1} K at 340 K decreases slowly upon cooling to a $\chi_M T$ value of 0.60 cm^3 mol^{-1} K at 73.3 K, which then forms a plateau down to 11.2 K, whereupon it then decreases rapidly upon cooling, finally reaching a $\chi_M T$ value of 0.57 cm^3 mol^{-1} K at 5 K due to Zeeman splitting. The Co(II) ion is high spin at 123 and 273 K, as evidenced by the variable-temperature crystallographic measurements (vide supra), and we have little evidence in the $\chi_M T$ vs T plots of a spin-crossover

dx.doi.org/10.1021/ic5001057 | Inorg. Chem. 2014, 53, 5055−5066

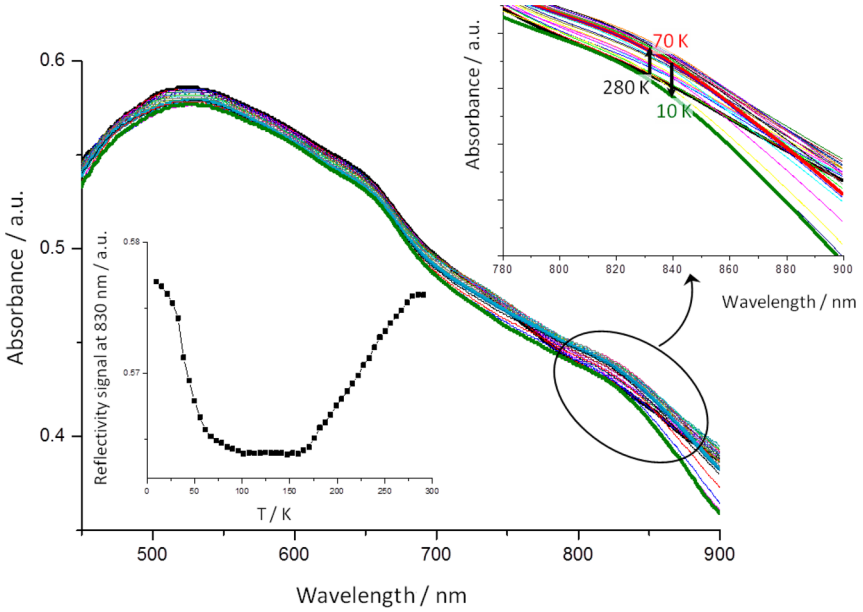

Figure 9. Optical reflectivity data for complex **1**, showing wavelength dependence of absorbance and temperature dependence of reflectivity at 830 nm (inset).

transition. Given that gradual Co(II) SCO transitions tend to be more curved in nature[31] in comparison to the $\chi_M T$ vs T profile for **2**, we have assumed that the Co(II) ion is in the high-spin state over the temperature range studied on the basis of the crystallographic measurements and linear nature of the $\chi_M T$ vs T profile. The low-temperature plateau $\chi_M T$ value of 0.60 $cm^3\ mol^{-1}\ K$ could result from a number of different exchange-coupled scenarios, the most likely involving antiferromagnetic exchange between the HS Co(II) ion and the two neutral radicals ($L^\bullet$) and subsequent ferromagnetic superexchange between the neutral radicals ($L^\bullet$) mediated via the HS Co(II) ion. The computed values from the DFT study (vide infra) offer a similar conclusion. Reasonable fits to the $\chi_M T$ vs T plot were not possible if we assumed an effective "$S = {}^1/_2$" for HS Co(II), which suggests, along with the residual $\chi_M T$ value of 0.60 $cm^3\ mol^{-1}\ K$ between 73.3 and 11.2 K, that any orbital angular momentum associated with the HS Co(II) ion is not quenched.

It is intriguing that **1** ($[Co^{II}(L^\bullet)_2](B(C_6F_5)_4)_2 \cdot CH_2Cl_2$) shows a clear spin-crossover transition while **2** ($[Co^{II}(L^\bullet)_2](B(C_6F_5)_4)_2 \cdot 2Et_2O$) remains high-spin throughout the temperature range studied when both compounds have identical coordination environments and anions but differ only in the type and amount of solvate present. Intermolecular effects,[32−35] important in propagating spin-crossover transitions, are effectively absent in **1** and **2** due to the nature of the ligand and anion used; therefore, the origin of any observed spin crossover must result from the role of the lattice solvate molecules and their influence on the crystal packing in **1** and **2**. As seen in Figure S3 (Supporting Information), the single dichloromethane solvate molecule in **1** confers a different packing arrangement to **2**, in which two diethyl ether solvate molecules lie in channels along the *b* axis. This results in shorter Co−Co intermolecular distances (Table 3) in **1** (11.738 Å at 123 K) in comparison to **2** (12.899 Å at 123 K) and, given the paucity of any other intermolecular pathway, must play a large role in the observed spin crossover in **1** and not **2**. Further experimental data are given in Optical Reflectivity Studies.

Optical Reflectivity Studies. To probe further the occurrence of spin crossover, reflectivity studies were carried out over the range 450−900 nm as a function of temperature, following the evolution of the absorption spectra and recording the reflectivity signal at a given wavelength. Variable-temperature measurements for **1** and **2** are reported in Figure 9 and Figure S15 in the Supporting Information, respectively. Absorption maxima for **1** are observed at 530, 630 (sh), and ∼830 (sh) nm. There are no previous visible spectral reports for $Co^{II}N_4O_2$ chromophores in $[M^{II}(L^\bullet)_2]$ species;[36] thus, we make tentative assignments for these bands by analogy to Hauser's work on $[Co(2,2'\text{-bipy})_3]^{2+}$ and $[Co(terpy)_2]^{2+}$ complexes.[37] The band at 830 nm, assigned to the ${}^4T_1 \rightarrow {}^4T_2$ transition of HS Co(II), increases in intensity with increasing temperature between 10 and 70 K and decreases in intensity between 70 and 280 K. The region between 450 and 650 nm, which shows very little dependence on temperature, is probably due to the ${}^2E \rightarrow {}^2T_1$; ${}^2T_2$ transitions of the low-spin form and MLCT bands. The decrease in reflectivity of the 830 nm band between 270 and 140 K is similar in shape to that in the $\chi_M T$ vs T plot (Figure 7) and is thus supportive of spin crossover occurring in **1**. What we cannot see in Figure 9 (left) (or in Figure S15 for **2**), in comparison to Fe^{II} crossover spectra, is the isosbestic behavior of HS and LS absorption bands, since these bands are much better separated and resolved for Fe^{II}.[38] The bands at 550 and 640 nm are better resolved in **2** and the absorbance of the 830 nm band is much more temperature dependent than in **1** with the reflectivity at 830 nm showing a temperature dependence that is similar to, but more curved than, the $\chi_M T$ vs T plot (Figure 8). Since the structural data and theory (below) strongly suggest that Co(II) in **2** remains high spin, the temperature dependence is likely to stem from a combination of magnetic exchange interactions, charge transfer, and temperature-dependent broadening effects, in a similar vein to that for $[Co(terpy)_2](PF_6)_2$.[37] Let us recall that reflectivity measurements are surface techniques, allowing only a small variation to be detected.

dx.doi.org/10.1021/ic5001057 | *Inorg. Chem.* 2014, 53, 5055−5066

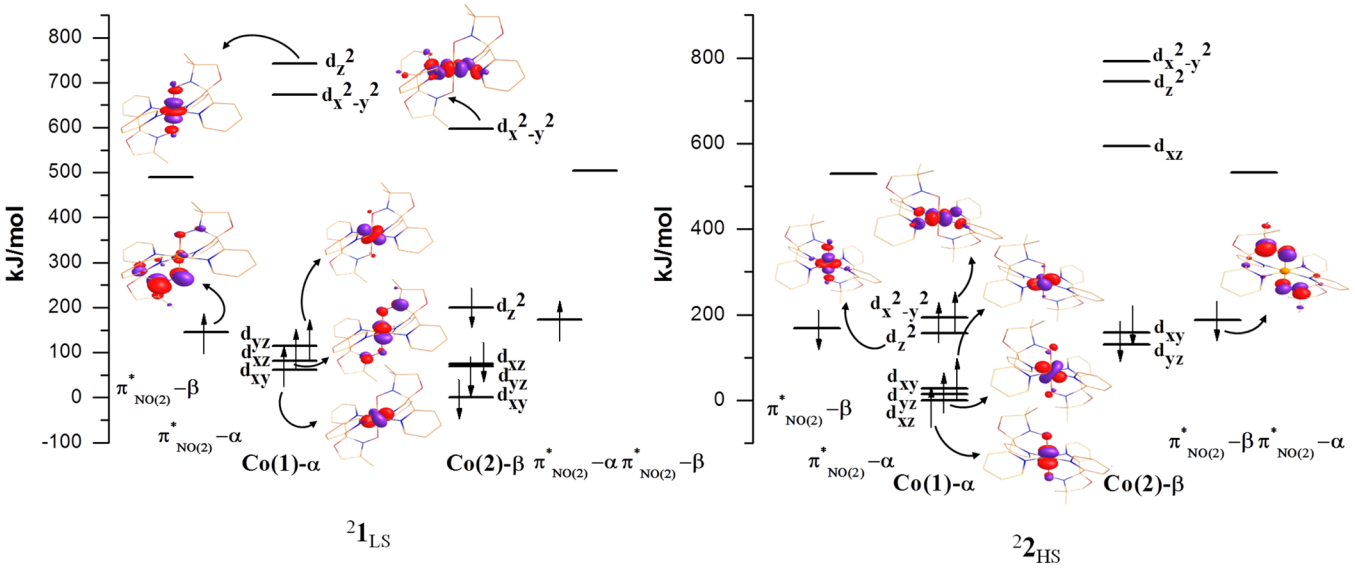

Figure 10. Eigenvalue plots along with the DFT computed energies for the $^2\mathbf{1}_{LS}$ and $^2\mathbf{2}_{HS}$ configurations.

We also explored light-induced excited state spin state trapping (LIESST) on the Squid magnetometer, for **2** in particular. From 405 to 980 nm, and particularly at 830 nm, we did not observe any changes in the magnetic signal. This is not surprising in view of the reflectivity data and the general lack of LIESST in Co^{II} SCO species.[37] Preparation of thin films of the sample or Zn(II) analogues could help us to further understand the optical behaviors observed.

Theoretical Studies. Our previous study on $[Co^{II}(L^{\bullet})_2](NO_3)_2$ (**3**),[12] the nitrate analogue of complexes **1** and **2** presented here, showed a strong ferromagnetic exchange between the low-spin Co^{II} ion and the nitroxide radical (J_1 = 63.8 cm^{-1}), which was rationalized by the orbital orthogonality between the d_{z^2} magnetic orbital on the low-spin Co^{II} ion d_{z^2} and the π^*_{NO} orbital(s) of the nitroxide radical. In addition to this the large and ferromagnetic radical−radical superexchange interaction observed in **3** (J_1 = 63.8 cm^{-1}) was due to a parallel alignment of the radical π^*_{NO} orbitals, leading to a small orbital overlap. The weak antiferromagnetic exchange between the low-spin Co^{II} ion and the nitroxide radical (J_1 = −0.512 cm^{-1}) in complex **1** is in stark contrast to the observations for **3** mentioned above. This raises a question of the origin of the difference in the exchange between the low-spin Co^{II} ion and the nitroxide radical in **3** (strongly ferromagnetic) and complex **1** (weakly antiferromagnetic). Unfortunately, crystallographic studies on **1** and **3** (Figure S4 and Table S1 in the Supporting Information) reveal no significant differences in any geometrical parameters for the cationic species when we consider the standard deviations; therefore, we have decided to carry out a detailed theoretical study on their structure and magnetic properties by analyzing the natural bonding orbitals and the overlap integral values to understand the extent of magnetic interaction present in these complexes and to correlate the magnetic exchange to any change in geometrical parameters.

The exchange parameters have been computed using the X-ray structures for both low-spin Co^{II} and high-spin Co^{II}. Two different exchange interactions have been assumed on the basis of the spin Hamiltonian $\hat{H} = -2J_1(\hat{S}_1\hat{S}_2 + \hat{S}_2\hat{S}_3) - 2J_2(\hat{S}_1\hat{S}_3)$ (where S_1 and S_3 are the radicals and S_2 is the Co^{II} ion). For low-spin Co^{II} the parameter set J_1 = +68.9 cm^{-1} and J_2 = 10.9 cm^{-1} has been obtained, resulting in a $S = {}^3/_2$ ground state, which is in contrast to the experimental observation in **1**, where the exchange parameters of J_1 = −0.512 cm^{-1} and J_2 = +138.7 cm^{-1} resulted in a $S = {}^1/_2$ ground state with the $S = {}^3/_2$ excited state 1.54 cm^{-1} higher in energy. The experimentally derived exchange parameters in the previously reported $[Co^{II}(L^{\bullet})_2](NO_3)_2$ (**3**)[12] were J_1 = +63.8 cm^{-1} and J_2 = +63.9 cm^{-1}, and the computed values were J_1 = +67.3 cm^{-1} and J_2= +15.1 cm^{-1}. In the case of high-spin Co^{II} the parameter set J_1 = −20.2 cm^{-1} and J_2 = 39.0 cm^{-1} has been obtained, which gives rise to an effective $S = {}^1/_2$ ground state with two $S = {}^3/_2$ states and one $S = {}^5/_2$ state lying 60.6, 179, and 161.6 cm^{-1}, respectively, above the ground state. The effective $S = {}^1/_2$ ground state obtained above matches the experimental observations (Figure 8) for complex **2**.

To probe the origin of these exchange interactions further, we have analyzed the electronic structure of the configurations $^2\mathbf{1}_{LS}$ (corresponding to **1**) and $^2\mathbf{2}_{HS}$ (corresponding to **2**), and the magnetic orbitals are shown in Figure 10. Our calculations on the $^2\mathbf{1}_{LS}$ configuration show that the unpaired electron in the low-spin Co^{II} ion is located in the d_{z^2} orbital, while the radical unpaired electrons are located in the π^*_{NO} orbitals. In $^2\mathbf{2}_{HS}$ the electronic configuration of the Co^{II} ion was determined to be $(d_{xy})^2(d_{yz})^2(d_{xz})^1(d_{z^2})^1(d_{x^2-y^2})^1$ with the unpaired electrons of the radicals found in the π^*_{NO} orbitals. Since the unpaired electron in the d_{xz} orbital in $^2\mathbf{2}_{HS}$ strongly interacts with the symmetry-compatible π^*_{NO} orbital(s), unlike the orthogonal e_g orbitals d_{z^2} and $d_{x^2-y^2}$, this leads to a moderate antiferromagnetic Co(II)−radical coupling. This results in a polarization mechanism leading to ferromagnetic radical−radical superexchange. The radical−radical coupling is enforced by the antiferromagnetic radical−Co(II) interactions: i.e., the strong $\pi^*_{NO(1)}-d_{xz}-\pi^*_{NO(2)}$ interaction enforces the same spin direction on the radical center, and this leads to a strong radical−radical ferromagnetic coupling. This suggests that the radical−radical coupling strength is directly correlated to the radical−Co(II) magnetic coupling, with stronger radical−Co(II) coupling likely to yield stronger radical−radical interactions. This is supported by the fact that, if the Co(II) ions are replaced by diamagnetic elements such as Zn(II), the magnetic coupling between the radical centers are essentially quenched, as witnessed earlier for the $[Zn^{II}(L^{\bullet})_2]$ case.[36]

dx.doi.org/10.1021/ic5001057 | Inorg. Chem. 2014, 53, 5055−5066

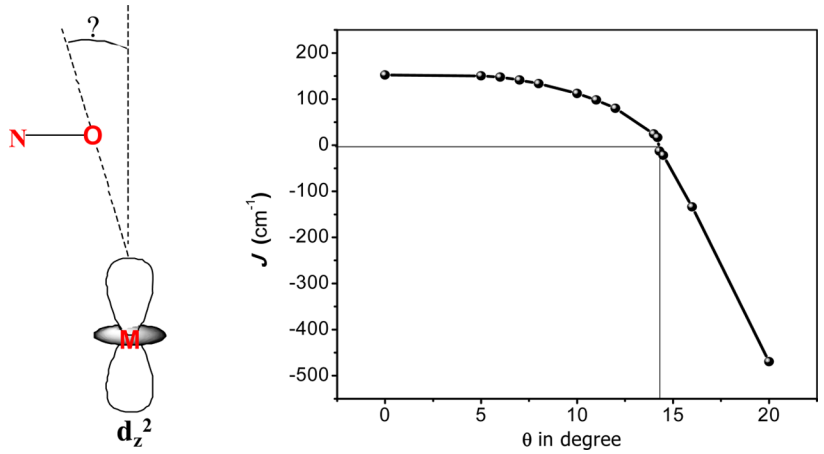

Figure 11. Representation of the tilt angle (θ) (left) and plot of magnetic exchange vs the tilt angle (θ) (right).

Previously, in the case of the $[Fe^{II}(L^{\bullet})_2](BF_4)_2$ complex[13] large antiferromagnetic coupling (-315 cm^{-1}) was observed experimentally between the radical centers, despite the fact that the intervening metal center was diamagnetic (LS Fe^{II}), whereas the radical coupling was essentially quenched as in the case of the $[Zn^{II}(L^{\bullet})_2]$ complex.[36] This suggests that a π-type interaction operates between the metal t_{2g} set of orbitals of Fe and the ligand π^*_{NO} antibonding orbital in the case of the Fe(II) and Co(II) radical systems, irrespective of their spin states. In the case of Zn(II), due to the completely filled d-orbital shell, such spin delocalization/polarization via an effective π interaction is not possible, thus leading to smaller exchange coupling constants.

While our calculations on **1** predict a set of exchange parameters similar to that of $[Co^{II}(L^{\bullet})_2](NO_3)_2$ (**3**)[12] the experimental $\chi_M T$ vs T fitting for complex **1** suggests the metal–radical coupling is weaker than the radical–radical coupling. To gain further insight into this, where even the sign of J_1 is computed to be incorrect, we have carefully analyzed the structure to see if there are any subtle structural distortions that may affect the strength and type of the exchange so dramatically. It may be expected that the relative orientation of the nitroxide radical N–O group in comparison to the central low-spin Co^{II} ion will have the most significant contribution to the magnitude and strength of the metal–radical exchange. On initial inspection, the difference between the average Co(1)–O(1)–N(3) bond angle of 114.07° in **1** in comparison to 115.4(2)° found in **3**[12] seems to be significant, but when we consider the standard deviations, they are effectively the same. Even though, crystallographically, there is little discernible difference between the structural parameters in **1** and **3**, we have decided to check the dependence of J_1 on the relative position of the nitroxide radical N–O group and have developed a magneto-structural correlation, where a strong dependence on the strength and sign of J_1 has been found.

When the angle θ (Figure 11) is varied from 0 to 20°, the magnitude of J_1 varies from +153 to -469 cm^{-1}, illustrating how strongly the J_1 parameter is correlated to this twist angle (Figure 11). To probe the origin of this interaction, we have computed the overlap integral between the Co(II) d_{z^2} orbital and the π^*_{NO} orbital (Table S2 in the Supporting Information), where the overlap integral between these two orbitals is found to increase as the twist angle increases. This can be easily rationalized; at $\theta = 0°$ the d_{z^2} orbital is essentially orthogonal to the π^*_{NO} orbital, but as θ increases, these two orbitals lose their orthogonality, leading to a decrease in the ferromagnetic coupling. At larger θ angles, due to substantial interaction with the d_{z^2} orbital, the interaction turns to antiferromagnetic. However, the fact remains that the huge value of the antiferromagnetic exchange constant after $\theta = 16°$ certainly could not be due to metal d_{z^2} and the ligand π^*_{NO} orbital overlap, as the deviation is very large. In those points, due to distortion in the structure, the d_{xz} and d_{yz} orbitals lie closer in energy to the d_{z^2} orbital, and this opens up a new π pathway for the interaction. Our MO plot also suggests a similar picture at larger θ angles (Figure 10).

Since such a twist angle is visible in complex **1** ($\theta = 1.2°$) and as this parameter is extremely sensitive to the magnitude of J, the discrepancy between the experiment and theory may be attributed due to the difference in the θ parameter, which is kept constant in our calculations.

The shape of the spin density on the LS Co(II) ion of the $^2\mathbf{1}_{LS}$ spin configuration (Figure 12) clearly indicates the d_{z^2} orbital. The estimated value of the spin density on the metal ion is -0.92, and in the radical sites it is 0.40 and 0.49, respectively, on the O and N atoms for the $^2\mathbf{1}_{LS}$ configuration. The spin density plot of the $^2\mathbf{1}_{LS}$ configuration suggests a strong spin delocalization on the equatorial pyridyl nitrogen atoms. The shape of the spin density on the HS Co(II) ion in the case of the $^2\mathbf{2}_{HS}$ configuration clearly indicates the possibility of a π-type interaction occurring between the metal d_{xz} orbital and the π^*_{NO} orbital of the ligand. Despite antiferromagnetic HS Co(II)–radical exchange, spin delocalization on the N–O bond

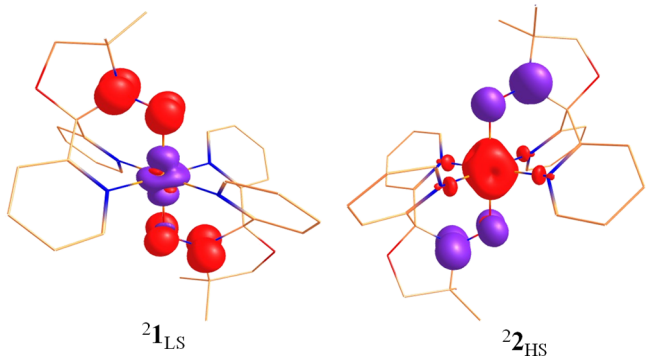

Figure 12. Computed spin density plots for the $^2\mathbf{1}_{LS}$ (for **1**) and $^2\mathbf{2}_{HS}$ (for **2**) configurations.

dx.doi.org/10.1021/ic5001057 | Inorg. Chem. 2014, 53, 5055–5066

rationalizes the strong ferromagnetic exchange among the radical centers.

CONCLUSION

The two novel oxazolidine nitroxide cobalt complexes $[Co^{II}(L^{\bullet})_2](B(C_6F_5)_4)_2\cdot CH_2Cl_2$ (**1**) and $[Co^{II}(L^{\bullet})_2](B(C_6F_5)_4)_2\cdot 2Et_2O$ (**2**), based on the 4,4-dimethyl-2,2-bis(2-pyridyl)oxazolidine *N*-oxide ($L^{\bullet}$) ligand, have been synthesized and structurally characterized by variable-temperature crystallographic studies. The central Co(II) ion in **1** undergoes a thermally activated gradual spin crossover, whereas the Co(II) ion in **2** remains high spin throughout. Complexes **1** and **2** both contain the neutral radical form of the ligand ($L^{\bullet}$), and there is no evidence of any reductively induced oxidation of the central Co(II) ion as previously reported.[12] This is expected by use of the tetrakis(pentafluorophenyl)borate anion in **1** and **2** instead of the redox-active tetraphenylborate used previously.[12] There is a clear solvate dependence on the spin-crossover properties, where complex **1** is a rare example of a compound that shows simultaneous exchange and spin crossover, the origin of which lies in the packing arrangements conferred by the different solvate molecules. Dramatic changes in electronic structure from solvent/solvate effects have been seen previously in the valence tautomeric (VT) cation $[Mn(cth)(diox)]^+$,[39a] which shows solvent-dependent electronic spectra, in $[Co(Me_2tpa)(DBCat)](PF_6)$,[39b] the ethanol solvate of which has a VT transition temperature 200 K greater than the toluene equivalent, and in $[Co^{III}(3,5\text{-}DBCat)(3,5\text{-}DBSQ)(py)_2]/[Co^{II}(3,5\text{-}DBSQ)2(py)_2]$,[39c] which shows a significant solvate dependence on the VT transition. Anion and solvate effects in complexes **1** and **2** result in different packing arrangements not only conferring a marked difference in the spin crossover properties but also showing a significant difference between the fitted J values of **1** in comparison to calculated (DFT broken symmetry) J values and to fitted J values on the previously reported complex $[Co^{II}(L^{\bullet})_2](NO_3)_2$ (**3**). A DFT theoretical study shows that this change is due to the sensitive influence of a tilt angle (θ) formed between the $Co(d_{z^2})$ orbital and the O atoms of the nitroxide NO radical moieties in $L^{\bullet}$. This suggests that the judicious choice of anion and solvate in these systems can dramatically affect the electronic structure of the complexes, allowing a tailored and flexible approach to their use in further application across the chemical sciences.

Finally, we note that the susceptibility plots in Figures 7 (top left) and 8 show some similarities to those reported for "spin triads" in Cu^{II} radical 1-D complexes of the type $[Cu(hfac)_2.L^R]_n$[40,41] that have spin state combinations $\{S = {}^1/_2{:}{}^1/_2{:}{}^1/_2\}$, as in the low-temperature form of complex **1**, the latter containing low-spin Co^{II}. Use of variable-temperature structural, EPR, and susceptibility methods showed that these Cu^{II}–radical complexes display "spin-crossover-like" thermal transitions between weakly exchange coupled states, WS, at high temperatures and strongly coupled states, SS (total spin ${}^1/_2$), at low temperatures. We believe that this proposal does not apply to complex **2**, since the high-spin Co^{II} structure does not vary with temperature. Likewise, spin crossover at the Co^{II} center of **1** is adequate to explain its behavior.

ASSOCIATED CONTENT

Supporting Information

Crystallographic information as.cif files. Figures S1 and S2 are TGA plots; Figure S3 shows packing diagrams; Figure S4 shows overlaid structures of **1** and **3**; Figures S5 to S10 are various fits of $\chi_M T$ vs T plots for **1** and best-fit contour map; Figures S11 to S13 are plots of magnetization isotherms for **1** and contour map of g vs D for giant spin $S = {}^3/_2$ Hamiltonian analysis; Figure S14 is a plot of $\chi_M T$ vs T as a function of D; Figure S15 shows optical reflectivity data for **2**. Table S1 is a comparison of geometrical parameters for **1** and **3**; Table S2 has computed overlap integrals. This material is available free of charge via the Internet at http://pubs.acs.org.

AUTHOR INFORMATION

Corresponding Author

*E-mail for K.S.M.: keith.murray@monash.edu.

Notes

The authors declare no competing financial interest.

ACKNOWLEDGMENTS

K.S.M. acknowledges the support of an Australian Research Council Discovery grant and, with G.R., the support of an Australia-India Strategic Research Fund grant. We thank Dr. Ayman Nafady for supplying $K(B(C_6F_5)_4)$ and for discussions and Nicholas Chilton for advice on program PHI.

REFERENCES

(1) Caneschi, A.; Gatteschi, D.; R. Sessoli, R.; Rey, P. *Acc. Chem. Res.* **1989**, *22*, 392–398.

(2) Caneschi, A.; Gatteschi, D.; Rey, P. *Prog. Inorg. Chem.* **1991**, *39*, 331–429.

(3) Caneschi, A.; Gatteschi, D.; Lalioti, N.; Sangregorio, C.; Sessoli, R.; Venturi, A.; Vindigni, A.; Rettori, A.; Pini, M. G.; Novak, M. A. *Angew. Chem., Int. Ed.* **2001**, *40*, 1760–1763.

(4) (a) Inoue, K.; Iwamura, H. *J. Am. Chem. Soc.* **1994**, *116*, 3173–3174. (b) Inoue, K.; Iwamura, H. *Adv. Mater.* **1996**, *8*, 73–76. (c) Inoue, K.; Hayamizu, T.; Iwamura, H.; Hashizume, D.; Ohashi, Y. *J. Am. Chem. Soc.* **1996**, *118*, 1803–1804.

(5) (a) Luneau, D.; Rey, P. In *Magnetism: A Supramolecular Function*; Kahn, O., Ed.; Kluwer Academic: Dordrecht, The Netherlands, 1996; NATO ASI Series *484*; pp 431–452. (b) Luneau, D.; Romero, F. M.; Ziessel, R. *Inorg. Chem.* **1998**, *37*, 5078–5087. (c) Fegy, K.; Luneau, T.; Ohm, C.; Paulsen, P.; Rey, P. *Angew. Chem., Int. Ed.* **1998**, *37*, 1270–1273.

(6) (a) Chirik, P. J.; Wieghardt, K. *Science* **2010**, *327*, 794–795. (b) Bowman, A. C.; Milsmann, C.; Bill, E.; Lobkovsky, E.; Weyermuller, T.; Wieghardt, K.; Chirik, P. J. *Inorg. Chem.* **2010**, *49*, 6110–6123. (c) Bart, S. C.; Lobkovsky, E.; Chirik, P. J. *J. Am. Chem. Soc.* **2004**, *126*, 13794–13807. (d) Pierpont, C. G.; Lange, C. W. *Prog. Inorg. Chem.* **1994**, *41*, 331–442. (e) Chaudhuri, P.; Wieghardt, K. *Prog. Inorg. Chem.* **2001**, *50*, 151–216. (f) Chaudhuri, P.; Verani, C. N.; Bill, E.; Bothe, E.; Weyhermuller, T.; Wieghardt, K. *J. Am. Chem. Soc.* **2001**, *123*, 2213–2223. (g) Sproules, S.; Wieghardt, K. *Coord. Chem. Rev.* **2010**, *254*, 1358–1382.

(7) Galyametdinov, Y.; Ksenofontov, V.; Prosvirin, A.; Ovchinnikov, I.; Ivanova, G.; Gutlich, P.; Haase, W. *Angew. Chem., Int. Ed.* **2001**, *40*, 4269–4271.

(8) Halder, G. J.; Kepert, C. J.; Moubaraki, B.; Murray, K. S.; Cashion, J. D. *Science* **2002**, *298*, 1762–1765.

(9) Clemente-León, M.; Coronado, E.; López-Jordá, M.; Waerenborgh, J. C. *Inorg. Chem.* **2011**, *50*, 9122–9130.

(10) Sutter, J.-P.; Fettouhi, M.; Li, L.; Michaut, C.; Ouahab, L.; Kahn, O. *Angew. Chem., Int. Ed.* **1996**, *35*, 2113–2116.

(11) Brooker, S.; Plieger, P. G.; Moubaraki, B.; Murray, K. S. *Angew. Chem., Int. Ed.* **1999**, *38*, 408–410.

(12) Gass, I. A.; Tewary, S.; Nafady, A.; Chilton, N. F.; Gartshore, C. J.; Asadi, M.; Lupton, D. W.; Moubaraki, B.; Bond, A. M.; Boas, J. F.; Guo, S. X.; Rajaraman, G.; Murray, K. S. *Inorg. Chem.* **2013**, *52*, 7557–7572.

dx.doi.org/10.1021/ic5001057 | *Inorg. Chem.* 2014, 53, 5055–5066

(13) Gass, I. A.; Gartshore, C. J.; Lupton, D. W.; Moubaraki, B.; Nafady, A.; Bond, A. M.; Boas, J. F.; Cashion, J. D.; Milsmann, C.; Wieghardt, K.; Murray, K. S. *Inorg. Chem.* **2011**, *50*, 3052−3064.
(14) Pal, P. K.; Chowdhury, S.; Drew, M. G. B.; Datta, D. *New. J. Chem.* **2002**, *26*, 367−371.
(15) Piers, W.; Chivers, T. *Chem. Soc. Rev.* **1997**, *26*, 345−354.
(16) Jensen, F. *Introduction to Computational Chemistry*, 2nd ed.; Wiley: Chichester, U.K., 2006
(17) Frisch, M. J., et al. *Gaussian 09, Revision A.02*; Gaussian, Inc., Wallingford, CT, 2009.
(18) Noodleman, L.; Peng, C. Y.; Case, D. A.; Mouesca, J. M. *Coord. Chem. Rev.* **1995**, *144*, 199−244.
(19) (a) Becke, A. D. *J. Chem. Phys.* **1986**, *84*, 4524−4529. (b) Perdew, J. P. *Phys. Rev. B* **1986**, *33*, 8822−8824.
(20) Berg, N.; Rajeshkumar, T.; Taylor, S. M.; Brechin, E. K.; Rajaraman, G.; Jones, L. F. *Chem. Eur. J.* **2012**, *18*, 5906−5918.
(21) (a) Rajeshkumar, T.; Saurabh, S. K.; Rajaraman, G. *Polyhedron* **2013**, *52*, 1299−1305. (b) Saurabh, S. K.; Neeraj, K. T.; Rajaraman, G. *Dalton Trans.* **2011**, *40*, 10897−10906. (c) Rajeshkumar, T.; Rajaraman, G. *Chem. Commun.* **2012**, *48*, 7856−7858. (d) Saurabh, S. K.; Rajaraman, G. *Dalton Trans.* **2013**, *42*, 3623−3630.
(22) Cremades, E.; Gomez-Coca, S.; Aravena, D.; Alvarez, S.; Ruiz, E. *J. Am. Chem. Soc.* **2012**, *134*, 10532−10542.
(23) (a) Tewary, S.; Gass, I. A.; Murray, K. S.; Rajaraman, G. *Eur. J. Inorg. Chem.* **2013**, 1024−1032. (b) Paulsen, H.; Duelund, L.; Winkler, H.; Toftlund, H.; Trautwein, A. X. *Inorg. Chem.* **2001**, *40*, 2201−2203. (c) Paulsen, H.; Paulsen, H.; Zimmermann, A.; Averseng, F.; Gerdan, M.; Winkler, H.; Toftlund, H.; Trautwein, A. X. *Monatsh. Chem.* **2003**, *134*, 295−306. (d) Krivokapic, I.; Zerara, M.; Daku, M. L.; Vargas, A.; Enachescu, C.; Ambrus, C.; Tregenna-Piggott, P.; Amstutz, N.; Krausz, E. *Coord. Chem. Rev.* **2007**, *251*, 364−378.
(24) (a) Schafer, A.; Horn, H.; Ahlrichs, R. *J. Chem. Phys.* **1992**, *97*, 2571−2577. (b) Schafer, A.; Huber, C.; Ahlrichs, R. *J. Chem. Phys.* **1994**, *100*, 5829−5835.
(25) Zhurko, G. A. *Chemcraft Version 1.6 (build 338)*; available from www.chemcraftprog.com.
(26) (a) Sheldrick, G. M. *SHELXL-97, program for refinement of crystal structures*; University of Göttingen, Göttingen, Germany, 1997. (b) Spek, A. L. *Acta Crystallogr., Sect. A* **1990**, *46*, C34.
(27) Spek, A. L. *J. Appl. Crystallogr.* **2003**, *36*, 7−13.
(28) Goodwin, H. A. *Top. Curr. Chem.* **2004**, *234*, 23−47.
(29) Kambe, K. *J. Phys. Soc. Jpn.* **1950**, *5*, 48−51.
(30) Chilton, N. F.; Anderson, R. P.; Turner, L. D.; Soncini, A.; Murray, K. S. *J. Comput. Chem.* **2013**, *34*, 1164−1175.
(31) Nielsen, P.; Toftlund, H.; Bond, A. D.; Boas, J. F.; Pilbrow, J. R.; Hanson, G. R.; Noble, C.; Riley, M. J.; Neville, S. M.; Moubaraki, B.; Murray, K. S. *Inorg. Chem.* **2009**, *48*, 7033−7047.
(32) (a) Yamada, M.; Ooidemizu, M.; Ikuta, Y.; Osa, S.; Matsumoto, N.; Iijima, S.; Kojima, M.; Dahan, F.; Tuchagues, J.-P. *Inorg. Chem.* **2003**, *42*, 8406−8416. (b) Matouzenko, G. S.; Molnar, G.; Brefuel, N.; Perrin, M.; Bousseksou, A.; Borshch, S. A. *Chem. Mater.* **2003**, *15*, 550−556. (c) Ikuta, Y.; Ooidemizu, M.; Yamahata, Y.; Yamada, M.; Osa, S.; Matsumoto, N.; Iijima, S.; Sunatsuki, Y.; Kojima, M.; Dahan, F.; Tuchagues, J.-P. *Inorg. Chem.* **2003**, *42*, 7001−7017. (d) Sunatsuki, Y.; Ikuta, Y.; Matsumoto, N.; Ohta, H.; Kojima, M.; Iijima, S.; Hayami, S.; Maeda, Y.; Kaizaki, S.; Dahan, F.; Tuchagues, J.-P. *Angew. Chem., Int. Ed* **2003**, *42*, 1614−1618.
(33) (a) Létard, J.-F.; Guionneau, P.; Codjovi, E.; Lavastre, O.; Bravic, G.; Chasseau, D.; Kahn, O. *J. Am. Chem. Soc.* **1997**, *119*, 10861−10862. (b) Hayami, S.; Gu, Z.-Z.; Shiro, M.; Einaga, Y.; Fujishima, A.; Sato, O. *J. Am. Chem. Soc.* **2000**, *122*, 7126−7127. (c) Boča, R.; Boča, M.; Dlháň, L.; Vrbová, M.; Werner, R. *Inorg. Chem.* **2001**, *40*, 3025−3033. (d) Real, J. A.; Gallois, B.; Granier, T.; Suez-Panamá, F.; Zarembowitch, J. *Inorg. Chem.* **1992**, *31*, 4972−4979. (e) Zhong, Z.-J.; Tao, J.-Q.; Yu, Z.; Duan, C.-Y.; Liu, Y.-J.; You, X.-Z. *J. Chem. Soc., Dalton Trans.* **1998**, 327−328.
(34) Hayami, S.; Shigeyoshi, Y.; Akita, M.; Inoue, K.; Kato, K.; Osaka, K.; Takata, M.; Kawajiri, R.; Mitani, T.; Maeda, Y. *Angew. Chem., Int. Ed.* **2005**, *44*, 4899−4903.
(35) Murray, K. S.; Kepert, C. J. *Top. Curr. Chem.* **2004**, *233*, 195−228.
(36) Ito, A.; Nakano, Y.; Urabe, M.; Tanaka, K.; Shiro, M. *Eur. J. Inorg. Chem.* **2006**, 3359−3368.
(37) Krivokapic, I.; Zerara, M.; Dakua, M. L.; Vargas, A.; Enachescu, C.; Ambrus, C.; Tregenna-Piggott, P.; Amstutz, N.; Krausz, E.; Hauser, A. *Coord. Chem. Rev.* **2007**, *251*, 364−378.
(38) Scott, H. S.; Ross, T. M.; Chilton, N. F.; Gass, I. A.; Moubaraki, B.; Chastanet, G.; Paradis, N.; Lètard, J. F.; Vignesh, K. R.; Rajaraman, G.; Batten, S. R.; Murray, K. S. *Dalton Trans.* **2013**, *42*, 16494−16509.
(39) (a) Caneschi, A.; Dei, A. *Angew. Chem., Int. Ed.* **1998**, *37*, 3005−3007. (b) Dapporto, P.; Dei, A.; Poneti, G.; Sorace, L. *Chem. Eur. J.* **2008**, *14*, 10915−10918. (c) Mulyana, Y.; Poneti, G.; Moubaraki, B.; Murray, K. S.; Abrahams, B. F.; Sorace, L.; Boskovic, C. *Dalton Trans.* **2010**, *39*, 4757−4767.
(40) Fedin, M.; Veber, S.; Gromov, I.; Maryunina, K.; Fokin, S.; Romanenko, G.; Sagdeev, R.; Ovcharenko, V.; Bagryanskaya, E. *Inorg. Chem.* **2007**, *46*, 11405−11415.
(41) Fedin, M.; Ovcharenko, V.; Sagdeev, R.; Reijerse, E.; Lubitz, W.; Bagryanskaya, E. *Angew. Chem., Int. Ed.* **2008**, *47*, 6897−6899.